Geophysical Research Letters

RESEARCH LETTER
10.1002/2018GL077230

Special Section:
Impact of the Sept. 10, 2017, solar event on Mars

The Morphology of the Solar Wind Magnetic Field Draping on the Dayside of Mars and Its Variability

Xiaohua Fang[1], Yingjuan Ma[2], Janet Luhmann[3], Yaxue Dong[1], David Brain[1], Dana Hurley[4], Chuanfei Dong[5], Christina O. Lee[3], and Bruce Jakosky[1]

[1]Laboratory for Atmospheric and Space Physics, University of Colorado Boulder, Boulder, CO, USA, [2]Department of Earth, Planetary, and Space Sciences, University of California, Los Angeles, CA, USA, [3]Space Sciences Laboratory, University of California, Berkeley, CA, USA, [4]Applied Physics Laboratory, The Johns Hopkins University, Laurel, MD, USA, [5]Department of Astrophysical Sciences and Princeton Plasma Physics Laboratory, Princeton University, Princeton, NJ, USA

Key Points:
- The clock angle of the field within the dayside magnetosheath is a reasonable proxy for the IMF
- The magnetic field clock angle departure increases with decreasing altitude and increasing SZA
- The draping direction departure is the greatest downstream of the quasi-parallel bow shock

Supporting Information:
- Supporting Information S1
- Movie S1

Correspondence to:
X. Fang,
Xiaohua.Fang@lasp.colorado.edu

Citation:
Fang, X., Ma, Y., Luhmann, J., Dong, Y., Brain, D., Hurley, D., et al. (2018). The morphology of the solar wind magnetic field draping on the dayside of Mars and its variability. *Geophysical Research Letters, 45*. https://doi.org/10.1002/2018GL077230

Received 20 JAN 2018
Accepted 20 MAR 2018
Accepted article online 26 MAR 2018

Abstract The magnetic field draping pattern in the magnetosheath of Mars is of interest for what it tells us about both the solar wind interaction with the Mars obstacle and the use of the field measured there as a proxy for the upstream interplanetary magnetic field (IMF) clock angle. We apply a time-dependent, global magnetohydrodynamic model toward quantifying the spatial and temporal variations of the magnetic field draping direction on the Martian dayside above 500-km altitude. The magnetic field and plasma are self-consistently solved over one Mars rotation period, with the dynamics of the field morphology considered as the result of the rotation of the crustal field orientation. Our results show how the magnetic field direction on the plane perpendicular to the solar wind flow direction gradually departs from the IMF as the solar wind penetrates toward the obstacle and into the tail region. This clock angle departure occurs mainly inside the magnetic pileup region and tailward of the terminator plane, exhibiting significant dawn-dusk and north-south asymmetries. Inside the dayside sheath region, the field direction has the greatest departure from the IMF-perpendicular component direction downstream of the quasi-parallel bow shock, which for the nominal Parker spiral is over the dawn quadrant. Thus, the best region to obtain an IMF clock angle proxy is within the dayside magnetosheath at sufficiently high altitudes, particularly over subsolar and dusk sectors. Our results illustrate that the crustal field has only a mild influence on the magnetic field draping direction within the magnetosheath region.

Plain Language Summary According to the classic magnetic field draping theory, when the solar wind plasma encounters unmagnetized planetary bodies, the entrained interplanetary magnetic field (IMF) would pile up and drape around as the flow is diverted. Under this approximation, the draped field lines maintain an orientation similar to the upstream IMF in the plane perpendicular to the solar wind flow direction. However, the real morphology of the magnetic field draping at Mars has been poorly understood. In this study, we apply a state-of-the-art global model to investigate the degree of distortion of the draped field lines when the complex Mars-solar wind interaction is self-consistently accounted for. Our results illustrate that when the IMF penetrates the magnetosheath edge into lower altitudes, the magnetic field lines may be so distorted and bent that their directions significantly deviate from the expectation from the classic field draping scenario. Our study reinforces the need to change any remaining notion of Mars in field line draping as a nonmagnetic planet. Moreover, this work presents a practical approach for inferring the IMF direction when direct measurements of the pristine solar wind are not available.

1. Introduction

In a classic magnetic field draping scenario for unmagnetized planetary bodies, the solar wind plasma is slowed down and diverted in the magnetosheath, resulting in the entrained interplanetary magnetic field (IMF) lines piling up and draping around the obstacles (e.g., Luhmann, 1986; Nagy et al., 2004). The draped field lines on the dayside away from the terminator generally are horizontal and maintain an orientation similar to the IMF in the plane perpendicular to the solar wind flow direction. Away from the IMF equatorial plane, the draped field lines slip over the obstacles and fill in the wakes of the induced magnetospheres (e.g., Luhmann et al., 2004). Such a simple picture, however, has been greatly complicated at Mars (Brain et al., 2006; Crider et al., 2004; Luhmann, Ma et al., 2015), due to its locally strong and highly nonuniform crustal magnetic fields

(Acuña et al., 1998). The details of the magnetic field distribution are important to realize the long-standing goal of understanding planetary ion transport and escape there. The involved physical processes include, but are not limited to, ion acceleration through the convection electric fields ($-\boldsymbol{U}_{sw} \times \boldsymbol{B}$; e.g., Dong, Fang, et al., 2015; Fang et al., 2008, 2010), the slingshot acceleration ($\boldsymbol{J} \times \boldsymbol{B}$; e.g., Dubinin et al., 2011; Tanaka, 1993), bulk plasma escape through flux rope detachment (e.g., Dubinin et al., 2008; Hara et al., 2014), plasma transport along open field lines (e.g., Haider, 1997; Liemohn et al., 2006; Ulusen & Linscott, 2008), and ionospheric density distributions (e.g., Ness et al., 2000).

The magnetic field in near-Mars space has been measured in situ by Phobos-2 (Riedler et al., 1989, 1991), Mars Global Surveyor (MGS; Acuña et al., 1998; Brain et al., 2006; Connerney et al., 2001; Crider et al., 2004; Espley et al., 2004), and the Mars Atmosphere and Volatile EvolutioN mission (MAVEN; Connerney et al., 2015; DiBraccio et al., 2017; Xu et al., 2017). However, its dynamic nature due to the variability of driving agents in the Mars-solar wind interaction, coupled with the planet's rotation, considerably limits the ability to obtain a global snapshot of the field distribution from satellite data. From this perspective, data-validated numerical models with plasma and field self-consistently calculated are particularly invaluable (Brecht, 1997; Dong, Bougher, et al., 2015; Kallio et al., 2006; Ma et al., 2004, 2014; Modolo et al., 2006). Although the model-calculated magnetic field has been presented either through 2-D planar/spherical/isosurface cuts or by showing example magnetic field line traces, the 3-D field evolution from the IMF interaction with the Mars obstacle is still poorly understood. In particular, there is a lack of a self-consistent and quantitative description of how the magnetic field draping direction changes over a broad spatial domain, and the extent to which it departs from the classic unmagnetized planet draping scenario. Such knowledge in turn is useful in practical application, as it relates to how confidently one may use magnetic field measurements downstream of the bow shock (BS) to infer the IMF direction. In fact, this study is motivated by the need from the MAVEN mission for reliable estimation of the IMF during September 2017 space weather events (see other papers of this special issue), when the spacecraft was unable to make direct upstream measurements due to its orbit limitation. The IMF direction is critical for inferring the direction of the convection electric field, which is extensively used in planetary ion escape studies (Brain et al., 2015; Y. Dong, Fang, et al., 2015). While the magnetic field distribution in the induced magnetosphere of Mars is subject to many factors (e.g., Liemohn et al., 2017; Luhmann, Dong et al., 2015), we focus our study on evaluating the magnetic field draping pattern as the planet rotates under quiet solar conditions with the most common IMF orientation.

2. Numerical Approach: Time-Dependent MHD

We adopt the 3-D multispecies, single-fluid magnetohydrodynamic (MHD) model of Ma et al. (2014), which self-consistently solves the solar wind and planetary plasma and magnetic field in a time-dependent fashion and has been shown to provide simulated time series that resemble MGS observations. Readers are referred to Ma et al. (2004, 2014) for the details of the MHD equations and numerical schemes; here we only describe basic model setup and input conditions that are needed for interpretation of our results. In this study we use exactly the same model run that has been discussed by Ma et al. (2014) and Fang et al. (2015, 2017). The run is carried out in the standard Mars-centered Solar Orbital (MSO) coordinate system. The simulation case is for a generic solar minimum configuration near autumn equinox ($F_{10.7}$ = 77 at 1 AU, L_s = 211.8), in which the upstream solar wind is stable with a density of 4 cm^{-3} and an antisunward speed of 400 km/s. The IMF is assumed to be along the nominal Parker spiral, specified by $|\boldsymbol{B}|$ = 3 nT and (B_X, B_Y, B_Z) = (1.6, −2.5, 0) nT. The Martian rotational axis is fixed at the direction of (−0.23, −0.36, 0.9), corresponding to a subsolar latitude of 13°S. The crustal magnetic field is specified using the Arkani-Hamed (2001) model, which is rotated by ∼1° every 4 min. The MHD equations are self-consistently and time-dependently solved for 26 hr (slightly over one Mars rotation period) within the entire domain (above 100-km altitude). The magnetic vector field solutions of this model were shown to agree reasonably well with actual observations by MGS along 12 orbits in May 2005 (Ma et al., 2014). The model-data agreement in the spatial and temporal distributions of the 3-D magnetic vector field forms the basis of the current study. It should be pointed out that by using single-fluid MHD approximation, our model is unable to account for the asymmetric distribution of the magnetic field with respect to the solar wind convection electric field direction, which has been noticed in hybrid model results (e.g., Kallio & Jarvinen, 2012; Modolo et al., 2006). However, it is unclear whether and to what degree the asymmetry exists in the magnetic field clock angle distribution. How the omission of the kinetic effects affects the conclusions of this work is a subject of interest for future study.

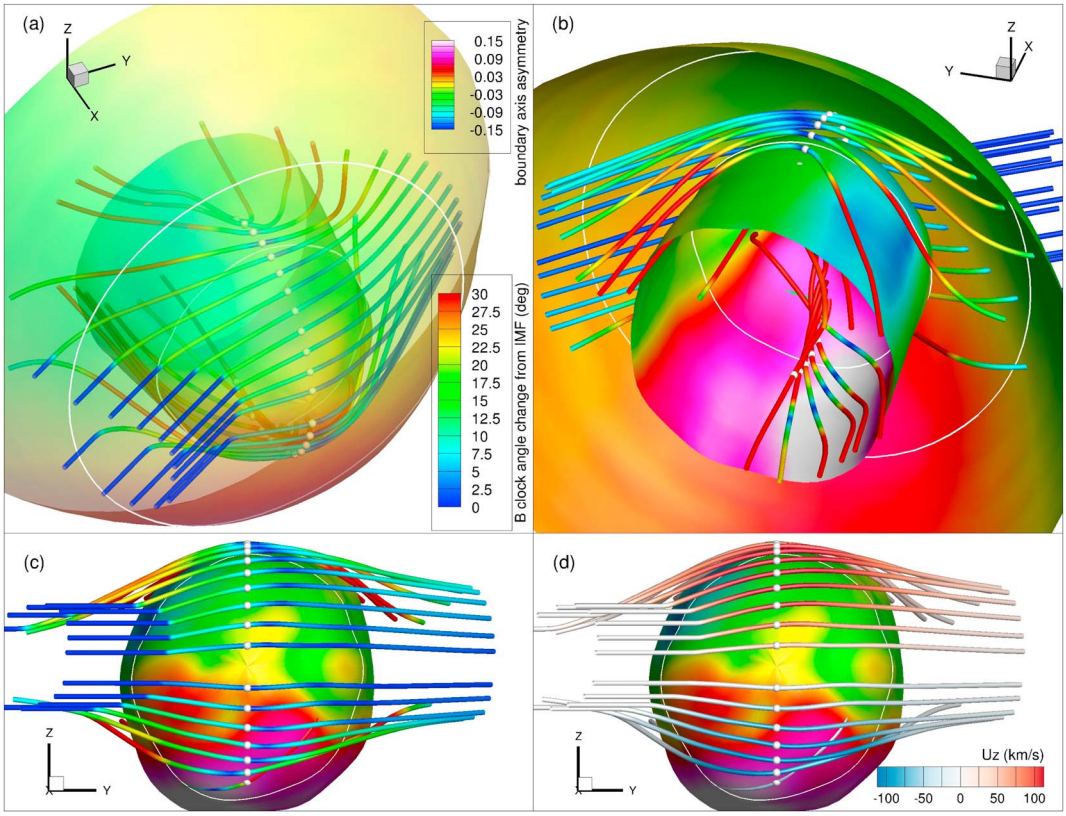

Figure 1. Example magnetic field lines at a time point within our time-dependent MHD simulation, viewed from different MSO perspectives. The field lines are traced from the points (marked as white dots) at 1,500-km altitude on the meridional plane spaced 10° apart in solar zenith angle from the subsolar point to solar zenith angle = 120°. The lines are color coded by the clock angle change of the local magnetic field from the interplanetary magnetic field (IMF) in panels (a)–(c), and by the Z_{MSO} component of the plasma velocity in panel (d). The model-derived bow shock and induced magnetospheric boundary/magnetic pileup boundary are shown for reference, with color indicating axis asymmetry of the boundaries (see the text). The white thin curves represent the intersection of the boundaries with the terminator plane.

It was noted by Brain et al. (2006) that the magnetic field draping direction at the MGS mapping altitude of 400 km is sensitive to the polarity of the IMF. In particular, it was found that a westward perpendicular IMF orientation (i.e., having $-Y_{MSO}$ component, like in the current study) would cause a more significant field distortion from an idealized magnetosheath draping pattern than an eastward IMF (having $+Y_{MSO}$ component). We therefore use the westward IMF in our simulation, with the aim of representing an upper bound on magnetic field distortions for the nominal, quiet solar wind interaction.

3. Model Results

Figure 1 shows example MHD-calculated magnetic field traces that pass through the dayside part of the meridional plane at 1,500-km altitude at a specific time of 8 UT, when the strongest crustal field has rotated to a local time near noon (see Figure 1 of Fang et al., 2015, for the time-varying crustal field orientation with respect to the Sun during the simulation time interval). The field lines in Figures 1a–1c are color coded by the magnitude of the local magnetic field clock angle departure from the value of the IMF. Here the clock angle ϕ is defined as the angle of the magnetic field, after being projected onto the MSO Y-Z plane, relative to the Y_{MSO} axis; that is, $\phi = 0°$ and 90° correspond to the projected directions parallel to Y_{MSO} and Z_{MSO}, respectively. In our simulation, the IMF has a clock angle of 180°.

In order to understand the magnetic field clock angle change, we superpose in Figure 1 the 3-D snapshots of the BS and induced magnetospheric boundary (IMB), which were determined by Fang et al. (2015, 2017) to be associated with plasma speed gradient peaks. The boundaries are color coded by their degree of asymmetry with respect to a nominal surface with rotation symmetry about the X_{MSO} axis, which is defined separately

for the BS and IMB as $(\rho(x,\theta) - \bar{\rho}(x))/\bar{\rho}(x)$, where x is the distance along the Sun-Mars line, θ is the azimuthal angle about the X axis, $\rho(x,\theta) = \sqrt{y^2 + z^2}$ is the boundary distance to the axis, and $\bar{\rho}(x)$ denotes the mean distance of $\rho(x,\theta)$ over θ. The magenta/white color indicates where the boundary is larger than average, green/blue where it is smaller, and yellow where it is close to average. Note that in the current study, we neglect subtle physical differences between what has been called the magnetic pileup boundary (MPB) and IMB and interchangeably use them. As can be seen in Figures 1a and 1b, most of the example start points for field line tracing sunward of the terminator plane are within the magnetosheath at this specific time point, providing an illustration of the magnetic field line draping and stretching within the transition region where the solar wind is dominant.

The magnetic field draping at high altitudes in Figure 1 generally meets the expectation from the classic draping scenario. The field lines gradually depart from the horizontal IMF projection (see Figure 1c for the view from the Sun) with increasing MSO latitude. Such a draping geometry is a natural consequence due to the deflection of the solar wind flow around the Martian obstacle (Crider et al., 2004). Figure 1d, where the field lines are color coded by the out-of-ecliptic (Z_{MSO}) velocity, shows that positive/negative U_z components are present in the northern/southern hemispheres, respectively, explaining the draping geometry. On the other hand, we observe in Figure 1 that the magnetic field clock angle diverges from its upstream counterpart as the solar zenith angle (SZA) increases. However, there are exceptions, one near the Mars-Solar-Electric field (MSE) equatorial plane (same as the MSO X-Y plane in this simulation), and the other near the MSE meridional plane but shifted duskward (see dark blue color regions of the field lines). This skewing is consistent with the Parker spiral IMF orientation we are using. These exceptions form cross-shaped areas having a minimum clock angle departure.

There are two caveats for the above inference from the examination of the example field line traces. First, the draped topology shown here happens within the magnetosheath region, while closed magnetic field lines are present (Luhmann, Ma, et al., 2015) and actually dominant at altitudes lower than 400 km (which is the MGS mapping altitude) in both numerical results and MAVEN observations (Xu et al., 2017). Second, the MHD results include complicated field line morphology (including an open topology connected to the nightside ionosphere, and stretched, closed field loops) in the Martian wake, which is not covered in this study but has been investigated elsewhere (e.g., Luhmann, Dong, et al., 2015; Xu et al., 2017).

Figure 2 quantifies the magnetic field clock angle departure from the IMF at various altitudes between 500 and 3,000 km, at the same time point as Figure 1. The blue and red shading indicates the areas with decreased and increased clock angles, respectively, which correspond to clockwise and counterclockwise rotations of the projected component of the magnetic field on the MSO Y-Z plane with respect to the $+X$ axis. A systematic clock angle change pattern is readily seen at altitudes higher than 1,500 km, consistent with the expectation from the classic draping geometry as presented in Figure 1. The pattern includes negative $\Delta\phi$ (i.e., field line clockwise rotation) in the north-dusk and south-dawn quadrants, and positive $\Delta\phi$ (i.e., field line counterclockwise rotation) in the north-dawn and south-dusk quadrants. Within these quadrants, the magnitude of $\Delta\phi$ tends to increase with increasing SZA as the tailward flowing solar wind together with the magnetic field are diverted by the planet. These quadrants are separated by cross-shaped white areas, where the magnetic field maintains a similar clock angle as the upstream IMF. The duskward skewing of the cross-shaped area is in accordance with a significant dawn-dusk asymmetry. It is seen that the clock angle of the field line on average departs more on the dawnside (which is downstream of the quasi-parallel BS in our case) than on the duskside (corresponding to the quasi-perpendicular BS). As demonstrated in Figures 1a and 1b, the magnetic field line downstream of the quasi-parallel BS undergoes more distortion to connect to the upstream IMF, making it harder for the field line to keep its original clock angle. It should be emphasized that it is more appropriate to refer the dawn-dusk asymmetry throughout this paper to the asymmetry between the sectors downstream of the quasi-parallel and quasi-perpendicular BSs, as the MSO and MSE coordinate systems do not necessarily overlap.

Another observation from Figure 2 is that $|\Delta\phi|$ tends to increase with decreasing altitude, as the penetrating solar wind and its entrained magnetic field are subject to greater perturbations from the obstacle. The regions with $|\Delta\phi| > 50°$ start to be more prevalent at altitudes lower than 1,000 km. Large clock angle departures basically happen in the vicinity of the MPB, which is particularly seen in Figures 2b and 2c in the places antisunward of the intersections of the MPB and selected altitude levels (marked by black dots). Moreover, the north-south asymmetry of $\Delta\phi$ is noticeable at altitudes lower than 2,000 km. It is worth noting that our MHD

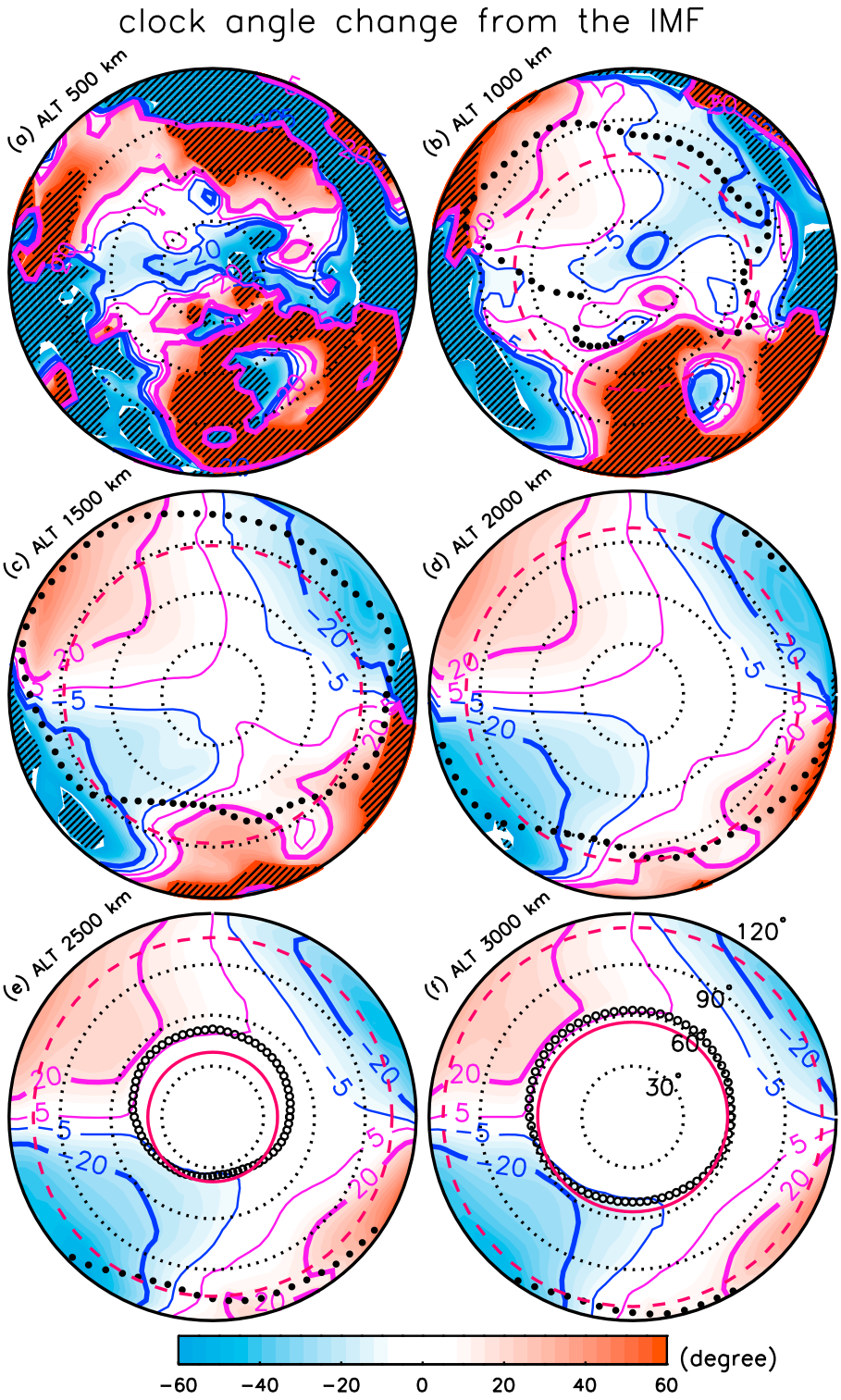

Figure 2. Clock angle departure of the dayside magnetic field from the interplanetary magnetic field (IMF) at the same time point as Figure 1. Panels (a-f) show the results at altitudes ranging from 500 km to 3000 km. The view is taken from the Sun, with the dawn and dusk to the left and right, respectively. The black inner dotted and outer solid circles show 30°, 60°, 90°, and 120° in solar zenith angle. The thin and thick contour lines mark 5° and 20° changes in the magnetic field clock angle, respectively. The shading with a fill pattern marks a large $\Delta\phi$ of more than 50° in magnitude. The red solid circle curves and black circle symbols in (e) and (f) mark intersection with the bow shock from the Vignes et al. (2000) and from the MHD results, respectively. The red dashed circle curves and black dot symbols in (b)–(f) mark interaction with the magnetic pileup boundary from the empirical and MHD results, respectively.

results imply that the crustal magnetic field influence is present everywhere at low altitudes. As illustrated by Fang et al. (2015, 2017), the crustal field extends its influence far beyond its geographical regions and is able to affect the shape and location of the BS. Consistent with the broad influence of the crustal field, it is seen in Figure 2a that the magnetic field dramatically departs from its original IMF direction at 500-km altitude over the entire dayside, including the northern hemisphere where there are no strong crustal field sources. This presumably results from the interaction between the solar wind and Mars (including the crustal field and induced currents in the ionosphere). Our MHD results suggest that great caution must be taken in approximating the IMF direction with the magnetic field draping direction at the MGS mapping altitude of 400 km as in previous studies, particularly when observational sites of interest reside within the magnetic pileup region (MPR).

Taking advantage of our time-dependent MHD results over one Mars rotation period, we investigate how the magnetic field draping direction dynamically changes as the crustal field orientation varies with respect to the stable impinging solar wind and IMF. A movie of the MHD results showing the dynamics of the field morphology as the result of the planet's rotation has been created and included in the supporting information of this paper. Our results are summarized in Figure 3. The probabilities for a X-ρ point being located inside the magnetosheath (Figure 3a) and inside the MPR (Figure 3e) distribute over broad spatial regions, which is the combined effect of the MPB and BS axis asymmetry and time variation of the boundary shapes and locations due to rotating crustal magnetic anomalies (Fang et al., 2015, 2017). Specifically, in Figure 3a, the spatial coverage of the probability of being inside the magnetosheath between 0 and 100% reflects how dramatically the locations of the MPB (the lower boundary of the sheath region; see the low-altitude part of the probability area) and the BS (see the high-altitude part) vary even under stable/quiet external solar wind conditions. The amount of scatter suggests caution when making a fit to the boundary locations using an axis symmetric assumption.

The 50th percentile, 75th percentile, and maximum values of $|\Delta\phi|$ are obtained when a X-ρ point is found to be located above the MPB (Figures 3b–3d) and below the MPB (Figures 3f–3h). Figure 3 illustrates a general pattern in the clock angle departure: $|\Delta\phi|$ tends to increase with decreasing altitude and increasing SZA. The magnetic field inside the sheath region has a much closer clock angle to the upstream IMF than inside the MPR. While on about half of occasions within the dayside MPR at high altitudes when the magnetic field departs from the IMF with a relative low value of <20° (Figure 3f), a considerable deviation almost always happens everywhere below the MPB (Figures 3h and 2a). This means that large uncertainties and errors may arise by using magnetic field measurements within the MPR to estimate the IMF direction. In contrast, inside the magnetosheath, $|\Delta\phi|$ is reasonably small even in the worst-case scenario as long as observational sites are sufficiently away from the planetary surface (Figure 3d). To make our results practically useful for guiding IMF direction estimation, we empirically derive a conic section surface ($X_0 = 0.51\ R_M$, $L = 1.46\ R_M$, and $\epsilon = 0.81$, marked by the thick solid curves in Figure 3). Any point above this empirical surface basically is inside the sheath region, where the magnetic field has a clock angle close to the IMF and the angular difference is lower than 20° at SZA $< \sim 55°$.

Because of finite clock angle departures and less interference from the crustal fields, it is the sheath region for which we focus our evaluation of the $\Delta\phi$ dawn-dusk and north-south asymmetries. While demonstrated in a snapshot in Figure 2, the asymmetries are further quantified by taking the time variability into account. As seen in Figure 4, we divide the magnetosheath results of Figures 3a and 3c into four quadrants: north-dawn (a and b), south-dawn (c and d), north-dusk (e and f), and south-dusk (g and h). These statistical results of the MHD model confirm that inside the sheath region the magnetic field has a systematically greater departure in its clock angle from the IMF on the dawnside than on the duskside, in association with different physical processes downstream of the quasi-parallel and quasi-perpendicular BSs, respectively. Due to strong crustal field distributions in the southern hemisphere, the magnetic field in the sheath region suffers a greater interference on its clock angle in the southern hemisphere than in the northern hemisphere. The north-south asymmetry, however, is not as remarkable as the dawn-dusk asymmetry. Moreover, the north-south asymmetry in the sheath region is more concentrated in the vicinity of the MPB, implying the limited capability of the crustal field in affecting the magnetic field clock angle at higher altitudes.

The Mars-solar wind interaction in this study is investigated under nominal, quiescent solar wind conditions. The dynamics of the magnetic field morphology, as demonstrated in Figures 3 and 4 and in the supporting information of the paper, is attributed to the continuous change of the crustal field orientation. Although this

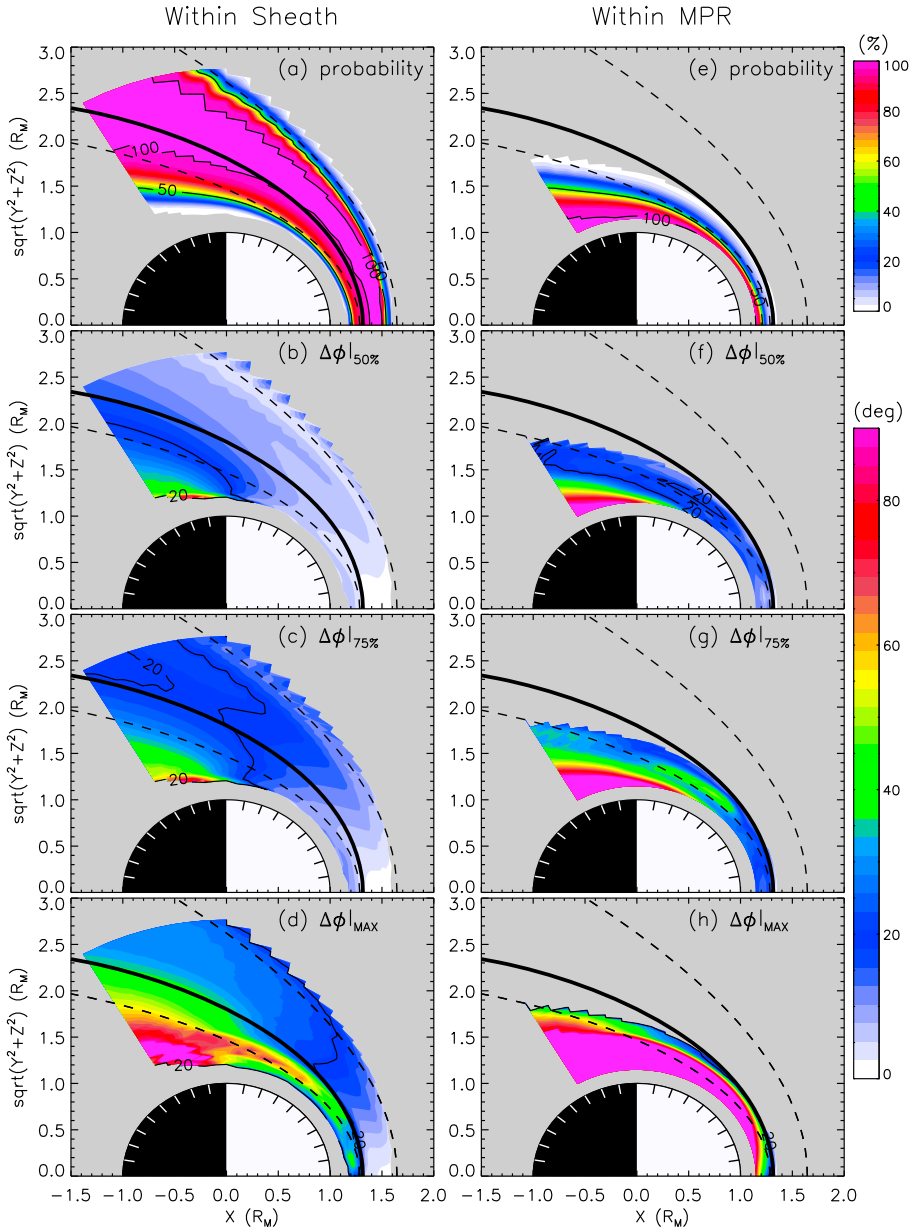

Figure 3. Panels (a) and (e) show the probabilities of a $X-\rho$ point being located in the magnetosheath region and within the magnetic pileup region (MPR), respectively. The probability at any given $X-\rho$ position is calculated by considering all spatial points rotating about the Sun-Mars line and also considering variation with time over a Mars rotation period. Panels (b)–(d) show the 50th percentile, 75th percentile, and maximum value in the magnetic field clock angle departure from the interplanetary magnetic field when a X-ρ point is within the magnetosheath. Panels (f)–(h) are similar to panels (b)–(d) but for the region within the MPR. All the calculation is conducted for the dayside (solar zenith angle $< 120°$) and for altitudes higher than 500 km above the planetary surface. The thick solid curve marks empirical locations, through which the magnetic field clock angle starts to significantly depart from its upstream value. The conic section parameters for our empirical fit are $X_0 = 0.51\ R_M$, $L = 1.46\ R_M$, and $\epsilon = 0.81$. The dashed curves indicate Vignes et al. (2000) bow shock and magnetic pileup boundary locations for reference.

work does not cover the scenario when the solar wind is disturbed particularly during space weather events, it is reasonably speculated that the variability of the upstream IMF would be closely reflected when it penetrates into the sheath region. If so, then the clock angle of the field within the dayside magnetosheath would still be able to provide a good measure for that of the IMF. It undoubtedly requires extensive follow-up studies to assess the robustness and the limitation of our model results in this paper.

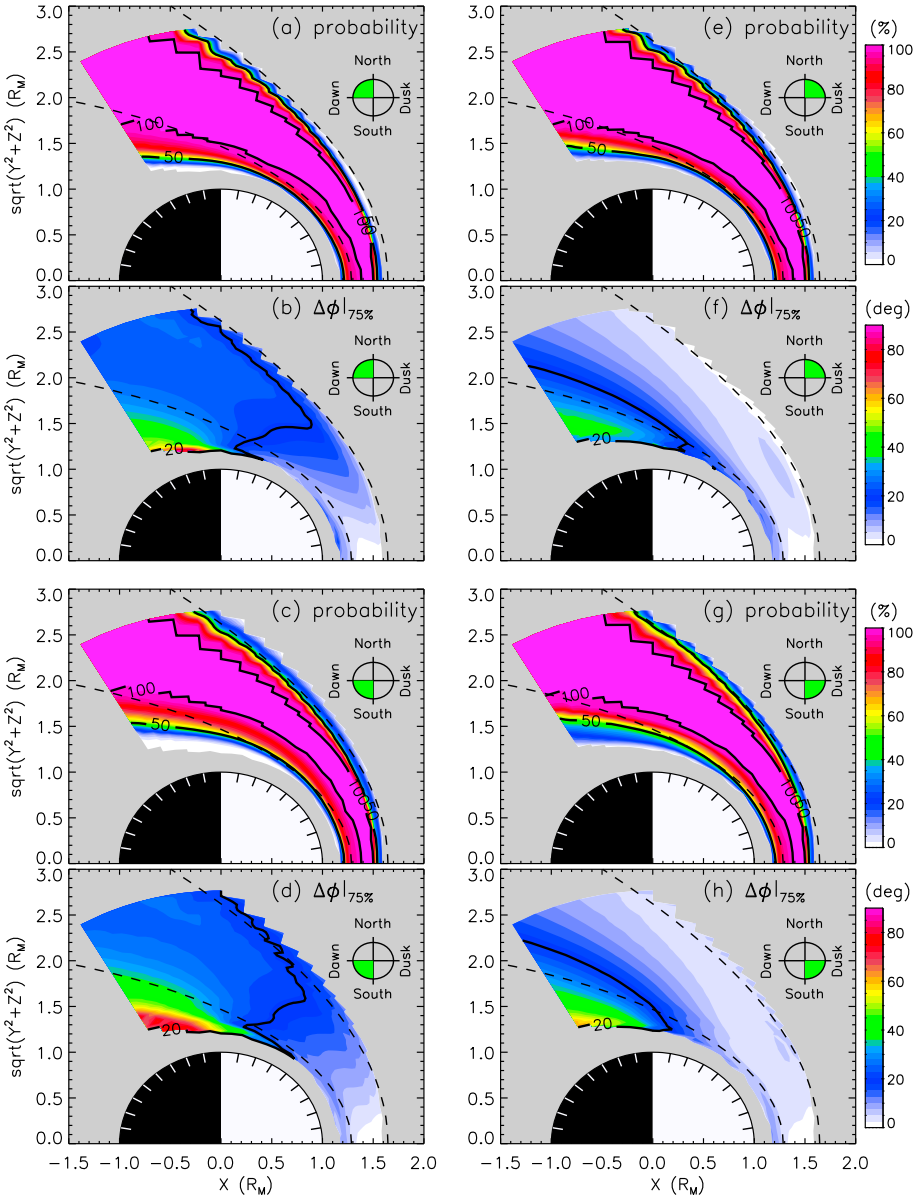

Figure 4. The probabilities of a X-ρ point being located in the magnetosheath region and the 75th percentile of the magnetic field clock angle departure from the interplanetary magnetic field when within the magnetosheath region, separately for the north-dawn quadrant (a and b), south-dawn quadrant (c and d), north-dusk quadrant (e and f), and south-dusk quadrant (g and h).

4. Concluding Remarks

Using the time-dependent, global MHD simulation results under quiet solar conditions, we characterize how the magnetic field draping direction (specifically its clock angle) evolves on the dayside of Mars. The change of the draping direction involves spatial variation in association with the large-scale solar wind-Mars interaction, as well as temporal variability due to continuously rotating crustal magnetic anomalies. While interaction processes are complicated and dynamic in nature, a simple picture may be deduced regarding the field line clock angle change that occur in the magnetosheath—distinguishing Mars from a purely unmagnetized planetary obstacle. In general, as the solar wind penetrates deeper and moves from the dayside toward the tail, the entrained magnetic field lines gradually depart from the clock angle of the upstream IMF. The field distortion becomes important and even severe particularly when the solar wind approaches the MPB. Nevertheless, our results suggest that the draping direction within the dayside magnetosheath region can serve as a

reasonably good proxy for the IMF clock angle in general at sufficiently high altitudes . An empirical conic section surface is provided for data scientists to infer the upstream IMF clock angle (and thus the convection electric field direction) when direct upstream measurements are unavailable.

One important finding of this study is that it is necessary to understand the context of a particular field measurement in order to evaluate its relationship to the IMF. Varying external (solar wind) and planetary (crustal field orientation) conditions result in a dynamic MPB, probably causing a location (particularly at relatively low altitudes) across the MPB back and forth between the sheath region and the MPR. Although clock angle changes with respect to the IMF are usually finite within the magnetosheath, large changes may happen within the MPR (including at high latitudes in the northern hemisphere where there are no strong crustal field sources). This suggests great caution in presuming that the magnetic field draping direction at the MGS mapping altitude of 400 km over weak crustal source regions is not significantly perturbed from the upstream IMF orientation. In addition, our results illustrate that the magnetic field clock angle change inside the sheath region has both a dawn-dusk asymmetry and a north-south asymmetry. The former is a consequence of the different magnetosheath field and flow geometries associated with regions dowstream of the quasi-parallel and quasi-perpendicular BSs, and the latter results from the nonuniform distribution of the crustal field over the planet. The dawn-dusk asymmetry (more precisely, the asymmetry between the sectors downstream of the quasi-parallel and quasi-perpendicular BSs) is suggested by the model to be more prominent than the north-south asymmetry in the sheath region. Our numerical analysis reinforces the need to change any remaining notions of Mars in field line draping as a nonmagnetic planet.

Acknowledgments
The work was supported by the NASA MAVEN project. Resources supporting the MHD simulation were provided by the NASA High-End Computing Program through the NASA Advanced Supercomputing Division at Ames Research Center. The MHD results are available at https://umich.box.com/s/cf59mr2ryrmwgklfs6v78gsv9v82zxg6.

References

Acuña, M. H., Connerney, J. E. P., Wasilewski, P., Lin, R. P., Anderson, K. A., Carlson, C. W., et al. (1998). Magnetic field and plasma observations at Mars: Initial results of the Mars Global Surveyor mission. *Science*, *279*, 1676–1680.

Arkani-Hamed, J. (2001). A 50-degree spherical harmonic model of the magnetic field of Mars. *Journal of Geophysical Research*, *106*, 23,197–23,208.

Brain, D. A., McFadden, J. P., Halekas, J. S., Connerney, J. E. P., Bougher, S. W., Curry, S., et al. (2015). The spatial distribution of planetary ion fluxes near Mars observed by MAVEN. *Geophysical Research Letters*, *42*, 9142–9148. https://doi.org/10.1002/2015GL065293

Brain, D. A., Mitchell, D. L., & Halekas, J. S. (2006). The magnetic field draping direction at Mars from April 1999 through August 2004. *Icarus*, *182*(2), 464–473.

Brecht, S. H. (1997). Hybrid simulations of the magnetic topology of Mars. *Journal of Geophysical Research*, *102*(A3), 4743–4750. https://doi.org/10.1029/96JA03205

Connerney, J., Acuña, M., Wasilewski, P., Kletetschka, G., Ness, N., Reme, H., et al. (2001). The global magnetic field of Mars and implications for crustal evolution. *Geophysical Research Letters*, *28*, 4015–4018.

Connerney, J. E. P., Espley, J. R., DiBraccio, G. A., Gruesbeck, J. R., Oliversen, R. J., Mitchell, D. L., et al. (2015). First results of the MAVEN magnetic field investigation. *Geophysical Research Letters*, *42*, 8819–8827. https://doi.org/10.1002/2015GL065366

Crider, D. H., Brain, D. A., Acuña, M. H., Vignes, D., Mazelle, C., & Bertucci, C. (2004). Mars Global Surveyor observations of solar wind magnetic field draping around Mars. *Space Science Reviews*, *111*, 203–221.

DiBraccio, G., Dann, J., Espley, J. R., Gruesbeck, J. R., Soobiah, Y., Connerney, J. E. P., et al. (2017). MAVEN observations of tail current sheet flapping at Mars. *Journal of Geophysical Research: Space Physics*, *122*, 4308–4324. https://doi.org/10.1002/2016JA023488

Dong, C., Bougher, S. W., Ma, Y., Toth, G., Lee, Y., Nagy, A. F., et al. (2015). Solar wind interaction with the Martian upper atmosphere: Crustal field orientation, solar cycle, and seasonal variations. *Journal of Geophysical Research: Space Physics*, *120*, 7857–7872. https://doi.org/10.1002/2015JA020990

Dong, Y., Fang, X., Brain, D. A., McFadden, J. P., Halekas, J. S., Connerney, J. E., et al. (2015). Strong plume fluxes at Mars observed by MAVEN: An important planetary ion escape channel. *Geophysical Research Letters*, *42*, 8942–8950. https://doi.org/10.1002/2015GL065346

Dubinin, E., Fraenz, M., Fedorov, A., Lundin, R., Edberg, N., Duru, F., & Vaisberg, O. (2011). Ion energization and escape on Mars and Venus. *Space Science Reviews*, *162*(1), 173–211. https://doi.org/10.1007/s11214-011-9831-7

Dubinin, E., Fraenz, M., Woch, J., Roussos, E., Winningham, J. D., Frahm, R. A., et al. (2008). Access of solar wind electrons into the Martian magnetosphere. *Annales de Geophysique*, *26*(11), 3511–3524. https://doi.org/10.5194/angeo-26-3511-2008

Espley, J. R., Cloutier, P. A., Brain, D. A., Crider, D. H., & Acuna, M. H. (2004). Observations of low-frequency magnetic oscillations in the Martian magnetosheath, magnetic pileup region, and tail. *Journal of Geophysical Research*, *109*, A07213. https://doi.org/10.1029/2003JA010193

Fang, X., Liemohn, M. W., Nagy, A. F., Luhmann, J. G., & Ma, Y. (2010). On the effect of the Martian crustal magnetic field on atmospheric erosion. *Icarus*, *206*, 130–138. https://doi.org/10.1016/j.icarus.2009.01.012

Fang, X., Liemohn, M. W., Nagy, A. F., Ma, Y., De Zeeuw, D. L., Kozyra, J. U., & Zurbuchen, T. H. (2008). Pickup oxygen ion velocity space and spatial distribution around Mars. *Journal of Geophysical Research*, *113*, A02210. https://doi.org/10.1029/2007JA012736

Fang, X., Ma, Y., Brain, D., Dong, Y., & Lillis, R. (2015). Control of Mars global atmospheric loss by the continuous rotation of the crustal magnetic field: A time-dependent MHD study. *Journal of Geophysical Research: Space Physics*, *120*, 10,926–10,944. https://doi.org/10.1002/2015JA021605

Fang, X., Ma, Y., Masunaga, K., Dong, Y., Brain, D., Halekas, J., et al. (2017). The Mars crustal magnetic field control of plasma boundary locations and atmospheric loss: MHD prediction and comparison with MAVEN. *Journal of Geophysical Research: Space Physics*, *122*, 4117–4137. https://doi.org/10.1002/2016JA023509

Haider, S. A. (1997). Chemistry of the nightside ionosphere of Mars. *Journal of Geophysical Research*, *102*, 407–416.

Hara, T., Seki, K., Hasegawa, H., Brain, D. A., Matsunaga, K., & Saito, M. H. (2014). The spatial structure of Martian magnetic flux ropes recovered by the Grad-Shafranov reconstruction technique. *Journal of Geophysical Research: Space Physics*, *119*, 1262–1271. https://doi.org/10.1002/2013JA019414

Kallio, E., Fedorov, A., Budnik, E., Säles, T., Janhunen, P., Schmidt, W., et al. (2006). Ion escape at Mars: Comparison of a 3-D hybrid simulation with Mars Express IMA/ASPERA-3 measurements. *Icarus*, *182*, 350–359.

Kallio, E., & Jarvinen, R. (2012). Kinetic effects on ion escape at Mars and Venus: Hybrid modeling studies. *Earth Planets and Space*, *64*(2), 157–163. https://doi.org/10.5047/eps.2011.08.014

Liemohn, M. W., Frahm, R. A., Winningham, J. D., Ma, Y., Barabash, S., Lundin, R., et al. (2006). Numerical interpretation of high-altitude photoelectron observations. *Icarus*, *182*(2), 383–395. https://doi.org/10.1016/j.icarus.2005.10.036

Liemohn, M. W., Xu, S., Dong, C., Bougher, S. W., Johnson, B. C., Ilie, R., & De Zeeuw, D. L. (2017). Ionospheric control of the dawn-dusk asymmetry of the Mars magnetotail current sheet. *Journal of Geophysical Research: Space Physics*, *122*, 6397–6414. https://doi.org/10.1002/2016JA023707

Luhmann, J., Ma, Y., Brain, D., Ulusen, D., Lillis, R., Halekas, J., & Espley, J. (2015). Solar wind interaction effects on the magnetic fields around Mars: Consequences for interplanetary and crustal field measurements. *Planetary and Space Science*, *117*, 15–23. https://doi.org/10.1016/j.pss.2015.05.004

Luhmann, J. G. (1986). The solar wind interaction with Venus. *Space Science Reviews*, *44*, 241–306.

Luhmann, J. G., Dong, C., Ma, Y., Curry, S. M., Mitchell, D., Espley, J., et al. (2015). Implications of MAVEN Mars near-wake measurements and models. *Geophysical Research Letters*, *42*, 9087–9094. https://doi.org/10.1002/2015GL066122

Luhmann, J. G., Ledvina, S. A., & Russell, C. T. (2004). Induced magnetospheres. *Advances in Space Research*, *33*, 1905–1912.

Ma, Y., Fang, X., Russell, C. T., Nagy, A. F., Toth, G., Luhmann, J. G., et al. (2014). Effects of crustal field rotation on the solar wind plasma interaction with Mars. *Geophysical Research Letters*, *41*, 6563–6569. https://doi.org/10.1002/2014GL060785

Ma, Y., Nagy, A. F., Sokolov, I. V., & Hansen, K. C. (2004). Three-dimensional, multispecies, high spatial resolution MHD studies of the solar wind interaction with Mars. *Journal of Geophysical Research*, *109*, A07211. https://doi.org/10.1029/2003JA010367

Modolo, R., Chanteur, G., Dubinin, E., & Matthews, A. P. (2006). Simulated solar wind plasma interaction with the Martian exosphere: Influence of the solar EUV flux on the bow shock and the magnetic pile-up boundary. *Annales de Geophysique*, *24*(12), 3403–3410.

Nagy, A. F., Winterhalter, D., Sauer, K., Cravens, T. E., Brecht, S., Mazelle, C., et al. (2004). The plasma environment of Mars. *Space Science Reviews*, *111*(1), 33–114. https://doi.org/10.1023/B:SPAC.0000032718.47512.92

Ness, N. F., Acuna, M. H., Connerney, J. E. P., Kliore, A. J., Breus, T. K., Krymskii, A. M., et al. (2000). Effects of magnetic anomalies discovered at Mars on the structure of the Martian ionosphere and solar wind interaction as follows from radio occultation experiments. *Journal of Geophysical Research*, *105*(A7), 15,991–16,004. https://doi.org/10.1029/1999JA000212

Riedler, W., Möhlmann, D., Oraevsky, V. N., Schwingenschuh, K., Yeroshenko, Y., Rustenbach, J., et al. (1989). Magnetic fields near Mars: First results. *Nature*, *341*, 604–607.

Riedler, W., Schwingenschuh, K., Lichtenegger, H., Mohlmann, D., Rustenbach, J., Yeroshenko, Y., et al. (1991). Interaction of the solar wind with the planet Mars: Phobos 2 magnetic field observations. *Planetary and Space Science*, *39*, 75–81.

Tanaka, T. (1993). Configurations of the solar wind flow and magnetic field around the planets with no magnetic field: Calculation by a new MHD simulation scheme. *Journal of Geophysical Research*, *98*, 17,251–17,262.

Ulusen, D., & Linscott, I. R. (2008). Low-energy electron current in the Martian tail due to reconnection of draped interplanetary magnetic field and crustal magnetic fields. *Journal of Geophysical Research*, *113*, E06001. https://doi.org/10.1029/2007JE002916

Vignes, D., Mazelle, C., Rme, H., Acuña, M. H., Connerney, J. E. P., Lin, R. P., et al. (2000). The solar wind interaction with Mars: Locations and shapes of the bow shock and the magnetic pile-up boundary from the observations of the MAG/ER Experiment onboard Mars Global Surveyor. *Geophysical Research Letters*, *27*(1), 49–52. https://doi.org/10.1029/1999GL010703

Xu, S., Mitchell, D., Liemohn, M., Fang, X., Ma, Y., Luhmann, J., et al. (2017). Martian low-altitude magnetic topology deduced from MAVEN/SWEA observations. *Journal of Geophysical Research: Space Physics*, *122*, 1831–1852. https://doi.org/10.1002/2016JA023467